



# Synergistic Hematite-Fullerene Electron-Extracting Layers for Improved Efficiency and Stability in Perovskite Solar Cells

Qinzhi Hou,<sup>[a]</sup> Jing Ren,<sup>[a]</sup> Haijun Chen,<sup>[a, b]</sup> Pan Yang,<sup>[c]</sup> Qian Shao,<sup>[d]</sup> Min Zhao,<sup>[e]</sup>  
Xiaochong Zhao,<sup>[c]</sup> Hongcai He,<sup>[a]</sup> Ning Wang,<sup>\*,[a, b]</sup> Qiang Luo,<sup>\*,[a]</sup> and Zhanhu Guo<sup>\*,[e]</sup>

Hematite,  $\alpha\text{-Fe}_2\text{O}_3$ , is arising as a promising electron-extraction material in perovskite solar cells, yet present  $\alpha\text{-Fe}_2\text{O}_3$ -based perovskite solar cells still show unsatisfactory efficiencies owing to large charge recombination. In this contribution, phenyl-C61-butyric acid methyl ester (PCBM) and  $\alpha\text{-Fe}_2\text{O}_3$  synergistically worked together as the electron transport layer (ETL) in planar heterojunction perovskite solar cells. The introduction of fullerene at the top of the  $\alpha\text{-Fe}_2\text{O}_3$  ETL improved the crystallinity of  $\text{CH}_3\text{NH}_3\text{PbI}_3$  perovskite and facilitated electron extraction. As a consequence, a substantially retarded charge recombination largely boosted the short-circuit current density and power conversion efficiency of perovskite solar cells. The optimized perovskite solar cells with  $\alpha\text{-Fe}_2\text{O}_3$ /PCBM ETL showed a competitive power conversion efficiency of 14.2%, which is 20% higher than that of pristine  $\alpha\text{-Fe}_2\text{O}_3$ -based solar cells. Moreover,  $\alpha\text{-Fe}_2\text{O}_3$ /PCBM-based perovskite solar cells exhibited improved stability compared to the pristine  $\alpha\text{-Fe}_2\text{O}_3$ -based devices, retaining over 95% of their initial values after 45 days storage in dark in humid air.

Metal halide perovskite solar cells have recently attracted tremendous attention since the seminal report by Miyasaka in 2009,<sup>[1]</sup> owing to their high power conversion efficiency, cheap raw materials and low-cost fabrication processes. With the continuous development of compositional engineering of perovskite light harvesters, optimized device interfaces and

charge transport materials, the certified power conversion efficiency of perovskite solar cells at present has been boosted up to 22.7%.<sup>[2–8]</sup> To date, perovskite solar cells are generally investigated into two device configurations, either P–I–N or N–I–P architectures. For N–I–P structured perovskite solar cells, perovskite light absorber is sandwiched between a n-type hole-blocking inorganic electron transport material (typically  $\text{TiO}_2$ ) and a p-type electron-blocking organic hole transport layer.<sup>[3,7]</sup>

Electron transporting layer (ETL) plays a vital role in charge extraction, electron transfer and hole-blocking, and thus strongly influences the charge separation and recombination in perovskite solar cells.<sup>[9–11]</sup> To date, vigorous efforts have been made to the development of high quality ETL with high electrical conductivity and appropriate energy levels for perovskite solar cells, such as  $\text{TiO}_2$ ,<sup>[12,13]</sup>  $\text{ZnO}$ ,<sup>[14,15]</sup>  $\text{SnO}_2$ ,<sup>[16,17]</sup> and  $\text{WO}_x$ .<sup>[18]</sup> Despite the progress on alternatives,  $\text{TiO}_2$  is still the most commonly used ETL and has achieved the recorded performance in planar perovskite solar cells thus far (~19%).<sup>[19]</sup> However, planar perovskite solar cells with the use of  $\text{TiO}_2$  as ETL usually suffer from serious hysteresis behavior and inferior stability.<sup>[20,21]</sup> In particular, perovskite solar cells fabricated with  $\text{TiO}_2$  ETL show fast performance degradation upon exposure to UV light illumination owing to the oxygen vacancies induced perovskite degradation.<sup>[22–24]</sup> Considering the above questions, our recent experimental results indicated that  $\alpha\text{-Fe}_2\text{O}_3$  compact layer emerged as a promising alternative to the conventional  $\text{TiO}_2$  for planar heterojunction perovskite solar cells.<sup>[25]</sup> Compared with conventional  $\text{TiO}_2$  ETL,  $\alpha\text{-Fe}_2\text{O}_3$  has a much lower conduction band level,<sup>[26]</sup> leading to a higher built-in potential across the perovskite layer and thus more efficient hole blocking ability at the interface between  $\text{CH}_3\text{NH}_3\text{PbI}_3/\alpha\text{-Fe}_2\text{O}_3$ .<sup>[25]</sup> As a consequence, perovskite solar cells fabricated with planar  $\alpha\text{-Fe}_2\text{O}_3$  ETL can obtain relatively low photocurrent hysteresis and good long-term stability. However, planar perovskite solar cells based on  $\alpha\text{-Fe}_2\text{O}_3$  ETL still suffer from relatively low power conversion efficiency (~12%), which can be mainly ascribed to large charge recombination arising from the short charge diffusion length and insufficient electron extracting ability. Logically, to avoid the poor charge transportation and ensure sufficient light transmittance,  $\alpha\text{-Fe}_2\text{O}_3$  ETL used in perovskite solar cells should be limited to a relatively thin thickness, while perovskite solar cells also suffered from insufficient electron extraction owing to the thin hematite ETL. Thus to boost device performance it is necessary to balance the charge transportation, electron extraction ability and light transmittance of  $\alpha\text{-Fe}_2\text{O}_3$  ETL. Organic transport layers, such as phenyl-C61-

[a] Q. Hou, J. Ren, H. Chen, H. He, Prof. N. Wang, Prof. Q. Luo  
State Key Laboratory of Electronic Thin Film and Integrated Devices  
University of Electronic Science and Technology of China  
Chengdu 610054, P.R. China  
E-mail: wangninguestc@gmail.com  
luo-q11@foxmail.com

[b] H. Chen, Prof. N. Wang  
State Key Laboratory of Marine Resource Utilization in  
South China Sea, Hainan University  
Haikou 570228, P.R. China

[c] P. Yang, X. Zhao  
Institute of Materials  
Chinese Academy of Engineering Physics  
Jiangyou 610200, P.R. China

[d] Prof. Q. Shao  
College of Chemical and Environmental Engineering  
Shandong University of Science and Technology  
Qingdao 266590, P.R. China

[e] M. Zhao, Prof. Z. Guo  
Integrated Composites Lab (ICL)  
Department of Chemical & Biomolecular Engineering  
University of Tennessee, Knoxville, Tennessee, 37966, USA  
E-mail: zguo10@utk.edu

butyric acid methyl ester (PCBM),<sup>[27]</sup> C<sub>60</sub> and their derivatives,<sup>[28,29]</sup> are excellent electron transport materials in organic solar cells and inverted P–I–N perovskite solar cells. The organic fullerene can promote electron extracting and reduce photocurrent hysteresis in inverted P–I–N perovskite solar cells.<sup>[30,31]</sup> However, when used as ETLs in normal N–I–P perovskite solar cells, fullerene cannot work as efficiently as n-type metal oxide ETLs due to their relatively smaller band gaps and insufficient hole-blocking ability. It is therefore highly desirable to combine metal oxide ETLs with fullerene to promote the electron extraction and hole-blocking ability of ETLs and thus suppress the interface recombination of normal N–I–P perovskite solar cells. In this study we demonstrate that the n-type PCBM combined with a thin  $\alpha$ -Fe<sub>2</sub>O<sub>3</sub> (~30 nm) could be used as efficient electron transport material in N–I–P planar perovskite solar cells with improved power conversion efficiency and superior stability. By depositing a layer of electron-extracting PCBM on the  $\alpha$ -Fe<sub>2</sub>O<sub>3</sub> film, the crystallinity of CH<sub>3</sub>NH<sub>3</sub>PbI<sub>3</sub> and the electron extraction ability of the  $\alpha$ -Fe<sub>2</sub>O<sub>3</sub>/PCBM ETL were enhanced, leading to significantly decreased charge recombination in the devices. Perovskite devices with  $\alpha$ -Fe<sub>2</sub>O<sub>3</sub>/PCBM ETL showed a competitive power conversion efficiency of 14.2%, 20% higher than that of pristine  $\alpha$ -Fe<sub>2</sub>O<sub>3</sub>-based solar cells. Moreover, perovskite devices also exhibited excellent stability, with an efficiency preservation of over 95% of their initial values after 45 days storage in humid air.

Planar perovskite solar cells were fabricated employing  $\alpha$ -Fe<sub>2</sub>O<sub>3</sub>/PCBM as ETL and spiro-OMeTAD as hole transport material (HTM), respectively. As shown in Figure 1a. PCBM was

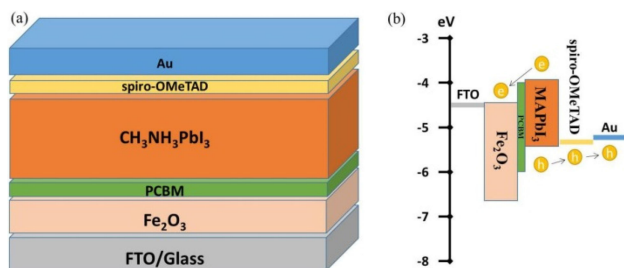


**Figure 1.** a) Device structure and b) the corresponding energy levels of the  $\alpha$ -Fe<sub>2</sub>O<sub>3</sub>/PCBM-based planar perovskite solar cells.

directly spin-coated on the surface of planar  $\alpha$ -Fe<sub>2</sub>O<sub>3</sub> ETL. The corresponding energy band level is shown in Figure 1b. Under irradiation, the photogenerated electrons on the CH<sub>3</sub>NH<sub>3</sub>PbI<sub>3</sub> conduction band inject into  $\alpha$ -Fe<sub>2</sub>O<sub>3</sub>/PCBM, while the holes in CH<sub>3</sub>NH<sub>3</sub>PbI<sub>3</sub> inject into the spiro-OMeTAD HTM. Figure 2a&b shows the representative top view SEM images of the as-deposited  $\alpha$ -Fe<sub>2</sub>O<sub>3</sub> and  $\alpha$ -Fe<sub>2</sub>O<sub>3</sub>/PCBM ETLs, respectively. It was found that the  $\alpha$ -Fe<sub>2</sub>O<sub>3</sub> inherited the FTO surface morphology and exhibited compact and continuous surface. From Raman spectroscopy measurement (inset of Figure 2a), the peaks located at 226, 295, and 496 cm<sup>-1</sup> can be respectively assigned to the A<sub>1g</sub>, E<sub>g</sub>, and E<sub>g</sub> Raman modes for the typical  $\alpha$ -Fe<sub>2</sub>O<sub>3</sub> phase, respectively.<sup>[32]</sup> By contrast, the surface of  $\alpha$ -Fe<sub>2</sub>O<sub>3</sub>/PCBM ETL was much smoother than that of  $\alpha$ -Fe<sub>2</sub>O<sub>3</sub> ETL, which would

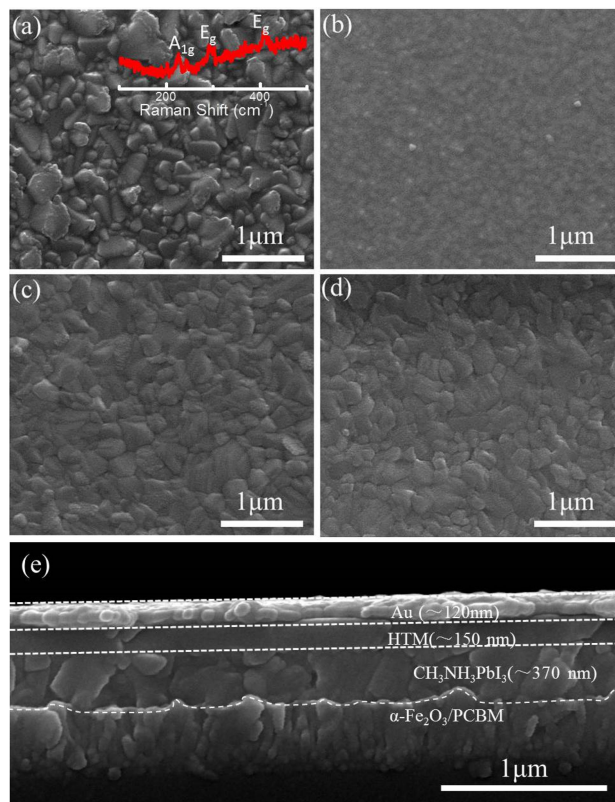


**Figure 2.** Top view SEM images of a)  $\alpha$ -Fe<sub>2</sub>O<sub>3</sub>- and b)  $\alpha$ -Fe<sub>2</sub>O<sub>3</sub>/PCBM-coated FTO substrates; SEM images of the CH<sub>3</sub>NH<sub>3</sub>PbI<sub>3</sub> perovskite films deposited on c)  $\alpha$ -Fe<sub>2</sub>O<sub>3</sub> and d)  $\alpha$ -Fe<sub>2</sub>O<sub>3</sub>/PCBM; e) cross-sectional SEM image of  $\alpha$ -Fe<sub>2</sub>O<sub>3</sub>/PCBM-based perovskite solar cells. Inset in Figure 2a is the Raman spectroscopy of the as-prepared  $\alpha$ -Fe<sub>2</sub>O<sub>3</sub> film.

lead to the reduced interface contact between  $\alpha$ -Fe<sub>2</sub>O<sub>3</sub>/PCBM and perovskite. Figure 2c&d shows the top view SEM images of the CH<sub>3</sub>NH<sub>3</sub>PbI<sub>3</sub> perovskite grown on the  $\alpha$ -Fe<sub>2</sub>O<sub>3</sub> and  $\alpha$ -Fe<sub>2</sub>O<sub>3</sub>/PCBM, respectively. Both  $\alpha$ -Fe<sub>2</sub>O<sub>3</sub> and  $\alpha$ -Fe<sub>2</sub>O<sub>3</sub>/PCBM-based perovskite films exhibited crack-free coverage, continuous and flat surfaces, as well as comparable crystal size (300–500 nm). Figure 2e shows the cross-sectional view SEM image of the device. The  $\alpha$ -Fe<sub>2</sub>O<sub>3</sub> ETL is difficult to be distinguished owing to the quite thin thickness (~30 nm). The thickness of perovskite active layer, HTM and Au top electrode is about 370 nm, 150 nm and 120 nm, respectively.

To investigate the impact of PCBM on CH<sub>3</sub>NH<sub>3</sub>PbI<sub>3</sub> growth, the crystallographic structure and phase purity of the as-deposited perovskite films were examined by X-ray diffraction (XRD), as shown in Figure 3a. The diffraction peaks at 14.0°, 28.4°, 31.9° and 40.4° can be unambiguously assigned to (110), (220), (310) and (224) faces of the tetragonal CH<sub>3</sub>NH<sub>3</sub>PbI<sub>3</sub> perovskite.<sup>[33,34]</sup> No additional peaks were observed from the XRD patterns, indicating the high purity of the perovskite. It is worth noting that the main peaks, (110) and (220), in the  $\alpha$ -Fe<sub>2</sub>O<sub>3</sub>/PCBM-based CH<sub>3</sub>NH<sub>3</sub>PbI<sub>3</sub> films are slightly stronger than those in the  $\alpha$ -Fe<sub>2</sub>O<sub>3</sub> based perovskite film, as shown in Figure 3b&c, suggesting that the perovskite deposited on  $\alpha$ -Fe<sub>2</sub>O<sub>3</sub>/PCBM substrate has a better crystallinity. During perovskite deposition, PCBM deposited on  $\alpha$ -Fe<sub>2</sub>O<sub>3</sub> ETL was partly

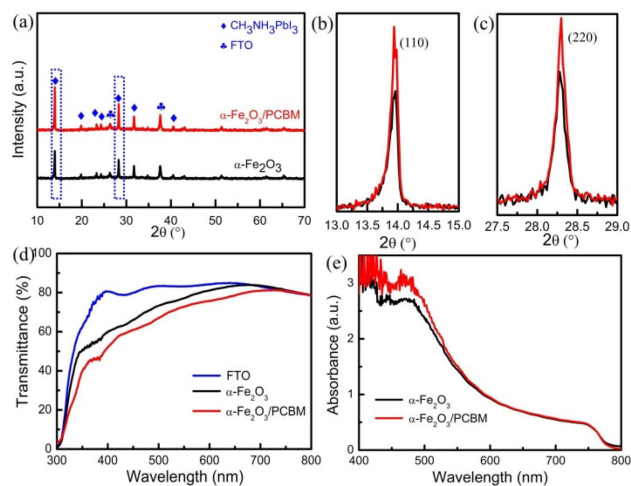


**Figure 3.** a) XRD patterns of perovskite films deposited on  $\alpha$ -Fe<sub>2</sub>O<sub>3</sub> and  $\alpha$ -Fe<sub>2</sub>O<sub>3</sub>/PCBM; b,c) the enlargement of the (110) and (220) peaks of perovskite films in (a), respectively. d) Transmission spectra of  $\alpha$ -Fe<sub>2</sub>O<sub>3</sub> and  $\alpha$ -Fe<sub>2</sub>O<sub>3</sub>/PCBM ETLs. e) Absorption spectra of perovskite films deposited on  $\alpha$ -Fe<sub>2</sub>O<sub>3</sub> and  $\alpha$ -Fe<sub>2</sub>O<sub>3</sub>/PCBM ETLs.

dissolved into *N,N*-dimethylformamide (DMF) solvent, which functioned as active sites for the nucleation and growth of perovskite and thus contributed to the improved crystallinity of CH<sub>3</sub>NH<sub>3</sub>PbI<sub>3</sub>.<sup>[35,36]</sup> Figure 3d shows the transmission spectra of the  $\alpha$ -Fe<sub>2</sub>O<sub>3</sub> and  $\alpha$ -Fe<sub>2</sub>O<sub>3</sub>/PCBM ETLs. After depositing a layer of  $\alpha$ -Fe<sub>2</sub>O<sub>3</sub> ETL on FTO substrate,  $\alpha$ -Fe<sub>2</sub>O<sub>3</sub>-based film demonstrated relatively low transmission in the short wavelength region owing to the relatively narrow band-gap of  $\alpha$ -Fe<sub>2</sub>O<sub>3</sub> (2.3 eV). When PCBM was spin-coated on  $\alpha$ -Fe<sub>2</sub>O<sub>3</sub> ETL, the  $\alpha$ -Fe<sub>2</sub>O<sub>3</sub>/PCBM film exhibited a slightly lower transmittance. Figure 3e shows the absorbance spectra of perovskite films deposited on  $\alpha$ -Fe<sub>2</sub>O<sub>3</sub> and  $\alpha$ -Fe<sub>2</sub>O<sub>3</sub>/PCBM. Both  $\alpha$ -Fe<sub>2</sub>O<sub>3</sub> and  $\alpha$ -Fe<sub>2</sub>O<sub>3</sub>/PCBM films exhibited almost identical absorption intensity except for small difference in the short-wavelength region. The absorption enhancement of  $\alpha$ -Fe<sub>2</sub>O<sub>3</sub>/PCBM based perovskite film at short wavelength region could originate from the parasitical absorption of PCBM.<sup>[37]</sup>

The photocurrent-voltage (*J-V*) curves of the as-fabricated planar perovskite solar cells using PCBM,  $\alpha$ -Fe<sub>2</sub>O<sub>3</sub> and  $\alpha$ -Fe<sub>2</sub>O<sub>3</sub>/PCBM as ETLs are shown in Figure 4a and Table 1. The perovskite solar cells fabricated with only PCBM achieved a low PCE of 7.31%, with an open-circuit voltage (*V*<sub>oc</sub>) of 0.94 V, a short-circuit density (*J*<sub>sc</sub>) of 14.5 mA cm<sup>-2</sup> and a fill factor (FF) of 53%. The relatively low PCE of the pristine PCBM-based solar cells could be ascribed to that the as-deposited PCBM would be mostly dissolved into DMF solvent during perovskite deposi-

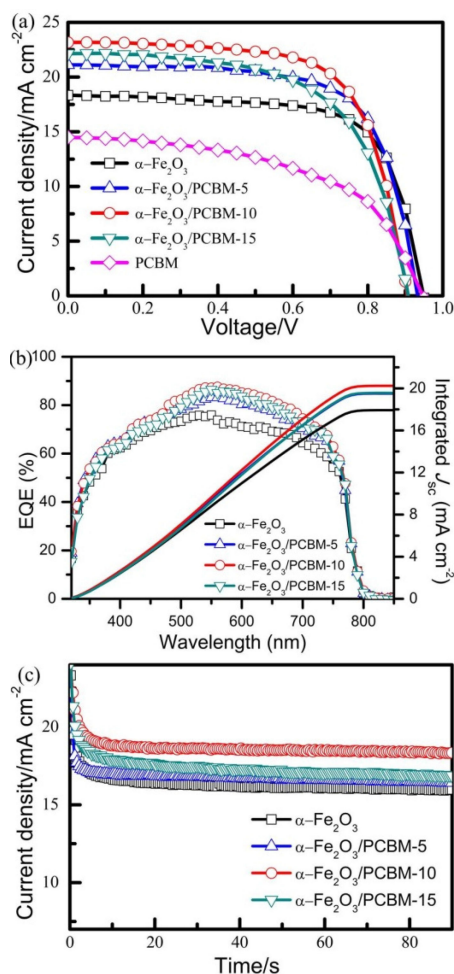


**Figure 4.** a) *J-V* curves and b) EQE spectra of the perovskite solar cells fabricated with different ETLs. c) The photocurrent density as a function of time for the cells held at a forward bias of the maximum output power points (0.65, 0.7, 0.7, and 0.7 V for the devices based on  $\alpha$ -Fe<sub>2</sub>O<sub>3</sub>,  $\alpha$ -Fe<sub>2</sub>O<sub>3</sub>/PCBM-5,  $\alpha$ -Fe<sub>2</sub>O<sub>3</sub>/PCBM-10, and  $\alpha$ -Fe<sub>2</sub>O<sub>3</sub>/PCBM-15 ETLs, respectively).

tion. And thus the PCBM layer cannot fully coverage the FTO glass surface, which would cause insufficient electron extraction and hole-blocking and result in low *J*<sub>sc</sub>, FF and PCE. The perovskite solar cells fabricated with  $\alpha$ -Fe<sub>2</sub>O<sub>3</sub> achieved a PCE of 12.1%, with a *V*<sub>oc</sub> of 0.95 V, a *J*<sub>sc</sub> of 18.3 mA cm<sup>-2</sup> and a FF of 70%. Impressively, when using  $\alpha$ -Fe<sub>2</sub>O<sub>3</sub>/PCBM as ETL, it was found that the *J*<sub>sc</sub> and PCE can be significantly improved. Perovskite solar cell modified with 5 mg mL<sup>-1</sup> PCBM ( $\alpha$ -Fe<sub>2</sub>O<sub>3</sub>/PCBM-5) displayed a *J*<sub>sc</sub> of 21.1 mA cm<sup>-2</sup>, resulting in an enhanced PCE of 13.6%. When the PCBM concentration was increased to 10 mg mL<sup>-1</sup> ( $\alpha$ -Fe<sub>2</sub>O<sub>3</sub>/PCBM-10), perovskite device

**Table 1.** Summary of device parameters of perovskite solar cells with different ETLs.

Solar cells	<i>J</i> <sub>sc</sub> [mA cm <sup>-2</sup> ]	<i>V</i> <sub>oc</sub> [V]	FF	PCE [%]
$\alpha$ -Fe <sub>2</sub> O <sub>3</sub>	18.3(18.0 ± 1.18)	0.95(0.93 ± 0.03)	0.70(0.66 ± 0.05)	12.1(11.2 ± 1.39)
$\alpha$ -Fe <sub>2</sub> O <sub>3</sub> /PCBM-5	21.1(20.8 ± 1.62)	0.94(0.93 ± 0.02)	0.68(0.66 ± 0.03)	13.6(12.9 ± 1.01)
$\alpha$ -Fe <sub>2</sub> O <sub>3</sub> /PCBM-10	23.2(22.5 ± 0.98)	0.91(0.90 ± 0.04)	0.68(0.66 ± 0.04)	14.2 (13.4 ± 0.99)
$\alpha$ -Fe <sub>2</sub> O <sub>3</sub> /PCBM-15	22.1(21.4 ± 1.05)	0.91(0.90 ± 0.03)	0.61(0.60 ± 0.03)	12.4(11.5 ± 0.88)
PCBM	14.5(14.0 ± 1.09)	0.94(0.90 ± 0.05)	0.53(0.52 ± 0.05)	7.3(6.6 ± 0.82)

achieved the best PCE of 14.2%, accompanied by a  $V_{oc}$  of 0.91 V, a  $J_{sc}$  of  $23.2 \text{ mA cm}^{-2}$  and a FF of 68%. Further increasing the PCBM concentration to  $15 \text{ mg mL}^{-1}$  ( $\alpha\text{-Fe}_2\text{O}_3/\text{PCBM-15}$ ), the  $J_{sc}$  decreased to  $22.2 \text{ mA cm}^{-2}$ , thereby leading to a decreased PCE of 13.1%. Therefore, it can be concluded that PCBM and  $\alpha\text{-Fe}_2\text{O}_3$  exert a synergic effect on the enhancement of device performance. Figure 4b shows the measured external quantum efficiency (EQE) spectra of the perovskite solar cells fabricated with pristine  $\alpha\text{-Fe}_2\text{O}_3$  and different  $\alpha\text{-Fe}_2\text{O}_3/\text{PCBM}$  ETLs. The integrated current densities based on these curves are 17.9, 19.5, 19.6 and  $20.3 \text{ mA cm}^{-2}$  for the perovskite solar cells fabricated with the  $\alpha\text{-Fe}_2\text{O}_3$ ,  $\alpha\text{-Fe}_2\text{O}_3/\text{PCBM-5}$ ,  $\alpha\text{-Fe}_2\text{O}_3/\text{PCBM-10}$  and  $\alpha\text{-Fe}_2\text{O}_3/\text{PCBM-15}$  ETL, respectively. Figure 4c exhibits the stabilized photocurrent output of  $\alpha\text{-Fe}_2\text{O}_3$  and  $\alpha\text{-Fe}_2\text{O}_3/\text{PCBM}$ -based perovskite solar cells examined under constant bias (close to their maximum power points). The photocurrent densities were stabilized to 15.9, 16.5, 18.3 and  $16.8 \text{ mA cm}^{-2}$ , yielding stabilized power conversion efficiency of 10.3%, 11.5%, 12.8% and 11.8% for  $\alpha\text{-Fe}_2\text{O}_3$ ,  $\alpha\text{-Fe}_2\text{O}_3/\text{PCBM-5}$ ,  $\alpha\text{-Fe}_2\text{O}_3/\text{PCBM-10}$  and  $\alpha\text{-Fe}_2\text{O}_3/\text{PCBM-15}$ -based perovskite solar cells, respectively.

To explore the reasons for the improved  $J_{sc}$  and PCE when  $\alpha\text{-Fe}_2\text{O}_3/\text{PCBM}$  is applied as ETL, the steady-state photoluminescence (PL) spectra of the perovskite films were investigated, as shown in Figure 5.  $\text{CH}_3\text{NH}_3\text{PbI}_3$  perovskite deposited on  $\alpha\text{-Fe}_2\text{O}_3$

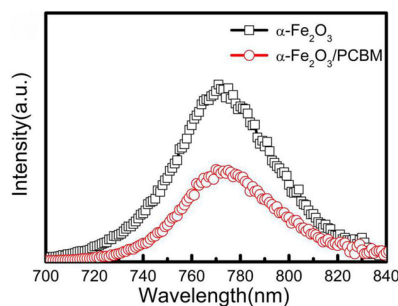


**Figure 5.** Steady PL spectra of perovskite films deposited on  $\alpha\text{-Fe}_2\text{O}_3$  and  $\alpha\text{-Fe}_2\text{O}_3/\text{PCBM}$  substrates.

and  $\alpha\text{-Fe}_2\text{O}_3/\text{PCBM}$  substrates exhibited the same emission peaks at about 770 nm. Generally, perovskite films with better crystallinity should generate higher PL intensity due to the reduced non-radiative recombination loss.<sup>[37]</sup> However, the PL emission intensity of  $\text{CH}_3\text{NH}_3\text{PbI}_3$  deposited on  $\alpha\text{-Fe}_2\text{O}_3/\text{PCBM}$  was lower than that on  $\alpha\text{-Fe}_2\text{O}_3$  ETL, which could be ascribed to high electron mobility PCBM that provides fast electron transport channels at the interface between perovskite and  $\alpha\text{-Fe}_2\text{O}_3$ . The charge recombination behavior of the perovskite solar cells was further characterized by impedance spectroscopy. Figure 6 exhibits the Nyquist plots of the as-fabricated perovskite solar cells with different ETLs measured at a forward bias of 0.7 V under AM 1.5G illumination (before measurement devices were subjected to light soaking for 10 min), in which two distinct semicircle arcs can be observed. In the order of decreasing frequency, the first semicircle arc at high frequency region is usually related to the interfacial charge transfer process, while

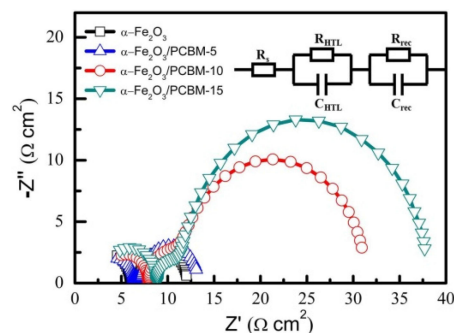


**Figure 6.** Nyquist plots of  $\alpha\text{-Fe}_2\text{O}_3$  and  $\alpha\text{-Fe}_2\text{O}_3/\text{PCBM}$ -based perovskite solar cells at a bias of 0.7 V under AM 1.5G illumination. Inset is the applied equivalent circuit diagram.

the second semicircle arc in low frequency region is ascribed to the charge recombination resistance ( $R_{rec}$ ) in the devices.<sup>[38–40]</sup> The  $R_{rec}$  is a useful parameter to evaluate the charge recombination process in perovskite solar cells. By fitting with the applied equivalent circuit (inset in Figure 6), the  $R_{rec}$  values of the  $\alpha\text{-Fe}_2\text{O}_3/\text{PCBM-5}$ ,  $\alpha\text{-Fe}_2\text{O}_3/\text{PCBM-10}$ , and  $\alpha\text{-Fe}_2\text{O}_3/\text{PCBM-15}$  based perovskite solar cells were  $6.2 \text{ } \Omega \text{ cm}^2$ ,  $20.7 \text{ } \Omega \text{ cm}^2$  and  $26.7 \text{ } \Omega \text{ cm}^2$ , respectively, significantly larger than that of the pristine  $\alpha\text{-Fe}_2\text{O}_3$ -based device ( $5.5 \text{ } \Omega \text{ cm}^2$ ) at 0.7 V under AM 1.5G illumination, indicating that the PCBM inserted between perovskite and  $\alpha\text{-Fe}_2\text{O}_3$  can efficiently retard the charge recombination. Considering that the ETL is the only different part in these cells, the decreased charge recombination can be attributed to the enhanced electron extraction induced by PCBM buffer layer. Moreover, PCBM dissolved during perovskite deposition will infiltrate into perovskite layer and passivate the perovskite grain boundaries, and thus facilitate electron transfer within perovskite film and at the  $\alpha\text{-Fe}_2\text{O}_3$ /perovskite interface.<sup>[30,31]</sup> Logically, when the concentration of PCBM was increased to  $15 \text{ mg mL}^{-1}$ , the increased recombination should result in the improved PCE for  $\alpha\text{-Fe}_2\text{O}_3/\text{PCBM-15}$ -based solar cells. However, the  $\alpha\text{-Fe}_2\text{O}_3/\text{PCBM-15}$ -based solar cells demonstrated decreased PCE owing to the lower current density. When PCBM concentration was relatively low ( $5 \text{ mg mL}^{-1}$ ), PCBM deposited on  $\alpha\text{-Fe}_2\text{O}_3$  would be partially dissolved in DMF during  $\text{CH}_3\text{NH}_3\text{PbI}_3$  deposition, leading to insufficient electron extraction due to the relatively thin thickness of PCBM. However, when the PCBM concentration was high ( $15 \text{ mg mL}^{-1}$ ), the thick PCBM will inevitably cause large charge transportation resistance and parasitic light absorption and thus lead to a decreased  $J_{sc}$  and PCE.

With regard to their commercial viability, the long-term stability of perovskite solar cells becomes as important as efficiency. The water-solubility of the perovskite makes perovskite devices highly prone to rapid performance degradation in humid environment.<sup>[41,42]</sup> The poor stability is unacceptable for practical applications. The long-term stability of the devices fabricated with  $\alpha\text{-Fe}_2\text{O}_3$  and  $\alpha\text{-Fe}_2\text{O}_3/\text{PCBM}$  ETL was firstly investigated as a function of storage time in dark under ambient conditions. As shown in Figure 7a, the PCE of  $\alpha\text{-Fe}_2\text{O}_3/\text{PCBM}$ -based perovskite solar cell preserved over 95% of its

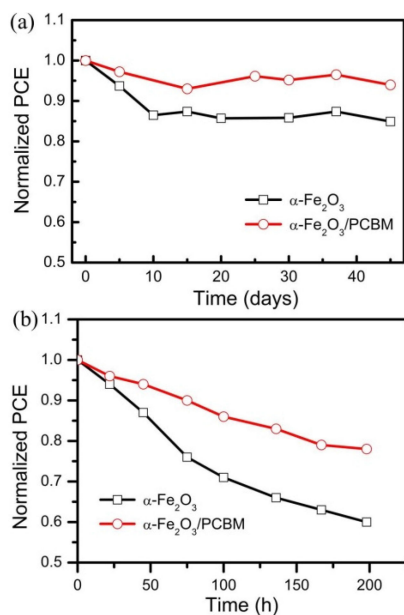


**Figure 7.** Efficiency stability of  $\alpha\text{-Fe}_2\text{O}_3$  and  $\alpha\text{-Fe}_2\text{O}_3/\text{PCBM}$ -based perovskite solar cells as a function of storage time: a) in dark in ambient atmosphere with an average relative humidity of 40% and b) under AM 1.5G light soaking in ambient atmosphere.

original value after 45 days storage in dark in humid air, while the devices fabricated on  $\alpha\text{-Fe}_2\text{O}_3$ -based ETL retained only 83% from their initial value, indicating that the incorporation of PCBM into the devices could efficiently improve the stability of the perovskite solar cells. Moreover, the photostability of the as-fabricated perovskite solar cells was also evaluated under AM 1.5G illumination (without ultraviolet filter). The perovskite solar cells fabricated with pristine  $\alpha\text{-Fe}_2\text{O}_3$  ETL decayed much faster than the device fabricated with  $\alpha\text{-Fe}_2\text{O}_3/\text{PCBM}$  ETL when subjected to AM 1.5G light soaking in air, the PCE decayed by 24% from its initial value after 100 h light soaking, and 40% of its initial value after 198 h. In sharp contrast, the  $\alpha\text{-Fe}_2\text{O}_3/\text{PCBM}$ -based solar cell demonstrated improved stability, preserving 90% of its original value after 100 h and slowly degrading to about 76% of its initial value after another 100 h. The higher photostability of  $\alpha\text{-Fe}_2\text{O}_3/\text{PCBM}$ -based perovskite solar cells could be attributed to the enhanced light absorption of PCBM in the UV light region and the improved crystalline of the perovskite film. The above results clearly demonstrate that the use of PCBM as electron extraction enhancer for  $\alpha\text{-Fe}_2\text{O}_3$ -based perovskite solar cells not only increased the output efficiency but also improved the long-term device stability.

In conclusion, we have demonstrated that the power conversion efficiency of perovskite solar cells fabricated with planar  $\alpha\text{-Fe}_2\text{O}_3$  ETL can be improved by modifying the  $\alpha\text{-Fe}_2\text{O}_3$  with a layer of thin PCBM. The introduction of fullerene atop the  $\alpha\text{-Fe}_2\text{O}_3$  ETL not only improved the crystallinity of  $\text{CH}_3\text{NH}_3\text{PbI}_3$  but also contributed to the improved electron extraction from perovskite, leading to the substantially retarded charge recombination of perovskite solar cells. Devices fabricated with  $\alpha\text{-Fe}_2\text{O}_3/\text{PCBM}$  achieved 20% enhancement in power conversion efficiency compared to the pristine  $\alpha\text{-Fe}_2\text{O}_3$ -

based solar cells. Moreover, perovskite solar cells modified by PCBM also showed better stability (95% vs 83%) than that of devices fabricated with un-modified  $\alpha\text{-Fe}_2\text{O}_3$  after 45 days storage in ambient atmosphere without any encapsulation. Our work provides a rational reference for realizing stable perovskite solar cells by combining metal oxide charge collecting layers with other organic charge extraction materials.

## Experimental Section

Fluorine-doped tin oxide (FTO)-coated glass sheets were etched with zinc powders and HCl to obtain the required electrode patterns. The etched FTO substrates were then washed sequentially with detergent, distilled water, ethanol, acetone and 2-propanol for 25 min, respectively. 0.1 M  $\text{Fe}(\text{NO}_3)_3 \cdot 9\text{H}_2\text{O}$  dissolved in ethanol was spun on the as-cleaned FTO glass at 6000 rpm for 40 s, followed by sintering at 300 °C for 1 h to form a thin  $\alpha\text{-Fe}_2\text{O}_3$  compact layer (~30 nm).  $\alpha\text{-Fe}_2\text{O}_3/\text{PCBM}$  ETLs were prepared by spin-coating PCBM chlorobenzene solution on  $\alpha\text{-Fe}_2\text{O}_3$  compact layer at a spin rate of 2000 rpm for 30 s and then annealed on a hotplate at 80 °C for 10 min in a glove box. Pristine PCBM ETL was prepared by spin-coating 10  $\text{mg mL}^{-1}$  PCBM on FTO glass at 2000 rpm for 30 s, and then annealed on a hotplate at 80 °C for 10 min in a glove box. Methyl ammonium iodide ( $\text{CH}_3\text{NH}_3\text{I}$ ) was synthesized through the reaction of 24 mL methylamine and 10 mL hydroiodic acid in 100 mL round bottomed flask at 0 °C.  $\text{CH}_3\text{NH}_3\text{I}$  can be successfully obtained by drying the recovered  $\text{CH}_3\text{NH}_3\text{I}$  white precipitate at 50 °C in vacuum oven for 24 h. A mixture of  $\text{CH}_3\text{NH}_3\text{I}$  (0.2 g) and  $\text{PbI}_2$  (0.578 g) was dissolved in 1 mL anhydrous *N,N*-dimethylformamide (DMF), followed by stirring at room temperature for 60 min to produce a clear  $\text{CH}_3\text{NH}_3\text{PbI}_3$  precursor solution.  $\text{CH}_3\text{NH}_3\text{PbI}_3$  perovskite film was deposited on  $\alpha\text{-Fe}_2\text{O}_3$ ,  $\alpha\text{-Fe}_2\text{O}_3/\text{PCBM}$  ETLs and PCBM coated FTO substrates by spin-coating 50  $\mu\text{L}$   $\text{CH}_3\text{NH}_3\text{PbI}_3$  precursor solution at 5000 rpm for 30 s. 150  $\mu\text{L}$  of anhydrous chlorobenzene was quickly dropped onto the surface during this process. The as-prepared films were immediately placed on a hot plate at 100 °C for 20 min. After the films were cooled down to room temperature, hole transport material (HTM) was subsequently spun on perovskite layer. HTM solution was prepared by adding 72.3 mg 2,2',7,7'-tetrakis(*N,N*-di-*p*-methoxyphenylamine)-9,9'-spiro-bifluorene (spiro-OMeTAD), 28.8  $\mu\text{L}$  4-*tert*-butylpyridine (TBP) and 17.5  $\mu\text{L}$  lithium bis(trifluoromethylsulphonyl) imide (Li-TFSI) solution (520  $\text{mg mL}^{-1}$  in acetonitrile) to 1 mL chlorobenzene. Then the spiro-OMeTAD coated films were stored in a drying oven for 12 h. The perovskite devices were completed by thermal evaporation of a 120 nm thick gold film as the top electrode.

## Characterization

X-ray diffraction (XRD) pattern data were recorded by using a Bede D1 X-ray diffractometer. The morphology of samples was characterized with Zeiss Merlin scanning electron microscope (SEM). The density-voltage (*J-V*) characteristics of perovskite solar cells were evaluated with a digital source meter (2400, Keithley Instruments, USA) under AM 1.5G illumination (100  $\text{mW cm}^{-2}$ ). The simulated light source was provided by a solar simulator (91192, Oriel, USA), which was calibrated by a standard silicon solar cell before measurements. Impedance spectroscopy measurements were taken at a bias of 0.7 V under AM 1.5G illumination. The amplitude of the modulation was 10 mV. The frequency range was 0.1 Hz to 100 kHz. The Z-view software was used to analyze the impedance data. The steady-state photoluminescence (PL) emission spectra were collected by using a fluorescence spectrometer instrument (FLS920, Edinburgh Instruments, UK). The PL spectra were collected

by illuminating the samples with a monochromatic light source with an excitation wavelength of 460 nm. The light source was provided by a pulsed xenon arc lamp. Transmission spectra and absorption spectra were measured by using an ultraviolet-visible spectrophotometer.

## Acknowledgements

This work was supported by the China-Japan International Cooperation Program Funds (No. 2010DFA61410 and 2011DFA50530), the National Natural Science Foundations of China (No. 51272037, 51272126, 51303116, and 51472043), Program for New Century Excellent Talents in University (No. NCET-12-0097), China Postdoctoral Science Foundation (No. 2017M622998) and the Science and Technology Foundation of Sichuan Province (2017JY0318).

## Conflict of Interest

The authors declare no conflict of interest.

**Keywords:** hematite • charge recombination • fullerene • perovskite solar cells • stability

- [1] A. Kojima, K. Teshima, Y. Shirai, T. Miyasaka, *J. Am. Chem. Soc.* **2009**, *131*, 6050–6051.
- [2] J. H. Im, C. R. Lee, J. W. Lee, S. W. Park, N. G. Park, *Nanoscale* **2011**, *3*, 4088–4093.
- [3] W. S. Yang, J. H. Noh, N. J. Jeon, Y. C. Kim, S. Ryu, J. Seo, S. I. Seok, *Science* **2015**, *348*, 1234–1237.
- [4] W. Ke, C. Xiao, C. Wang, C. Wang, B. Saparov, H. S. Duan, D. Zhao, Z. Xiao, P. Schulz, S. P. Harvey, W. Liao, W. Meng, Y. Yu, A. J. Cimaroli, C. S. Jiang, K. Zhu, M. A. J. G. Fang, D. B. Mitzi, Y. Yan, *Adv. Mater.* **2016**, *28*, 5214–5221.
- [5] N. J. Jeon, J. H. Noh, W. S. Yang, Y. C. Kim, S. Ryu, J. Seo, S. I. Seok, *Nature* **2015**, *517*, 476–480.
- [6] W. Nie, H. Tsai, R. Asadpour, J. C. Blancon, A. J. Neukirch, G. Gupta, J. J. Crochet, M. Chhwalla, S. Tretiak, M. A. Alam, H. L. Wang, A. D. Mohite, *Science* **2015**, *347*, 522–525.
- [7] D. Bi, T. Wolfgang, D. M. Ibrahim, P. Gao, J. Luo, R. Clementine, S. Kurt, A. Antonio, G. Fabrizio, C. B. Juan-Pablo, D. Jean-David, M. Z. Shaik, K. N. Mohammad, G. Michael, H. Anders, *Sci. Adv.* **2016**, *2*, 1501170.
- [8] Research Cell Efficiency Records, NREL, <http://www.nrel.gov/ncpv/>, accessed: December, 2017.
- [9] H. S. Kim, C. R. Lee, J. H. Im, H. S. Kim, C. R. Lee, J. H. Im, K. B. Lee, T. Moehl, A. Marchioro, S. J. Moon, R. Humphry-Baker, J. H. Yum, J. E. Moser, M. Grätzel, N. G. Park, *Sci. Rep.* **2012**, *2*, 591–596.
- [10] H. Tan, A. Jain, O. Voznyy, X. Lan, G. D. A. Fp, J. Z. Fan, R. Quintero-Bermudez, M. Yuan, B. Zhang, Y. Zhao, F. Fan, P. Li, L. N. Quan, Y. Zhao, Z. H. Lu, Z. Yang, S. Hoogl, E. H. Sargent, *Science* **2017**, *355*, 722–726.
- [11] S. S. Shin, E. J. Yeom, W. S. Yang, R. S. Hu, M. G. Kim, J. Im, J. Seo, J. H. Noh, S. I. Seok, *Science* **2017**, *356*, 167–171.
- [12] Y. Xiong, Y. Guo, Z. Xue, Z. Xue, P. Xu, M. He, B. Liu, *Nano Res.* **2015**, *8*, 1997–2003.
- [13] Y. Li, J. K. Cooper, W. Liu, C. M. Sutterfella, M. Amani, J. W. Beeman, A. Javey, J. W. Ager, Y. Liu, F. M. Toma, I. D. Sharp, *Nat. Commun.* **2016**, *7*, 12446–12450.
- [14] M. Khalid, S. B. Sankar, A. Aram, *Adv. Energy Mater.* **2015**, *5*, 1500568.
- [15] X. Zhao, H. Shen, Y. Zhang, X. Li, X. Zhao, M. Tai, J. Li, J. Li, X. Li, H. Lin, *ACS Appl. Mater. Interfaces* **2016**, *8*, 7826–7833.
- [16] L. Xiong, M. Qin, G. Yang, Y. Guo, H. Lei, Q. Liu, W. Ke, H. Tao, P. Qin, S. Li, H. Yu, G. Fang, *J. Mater. Chem. A* **2016**, *4*, 8374–8383.
- [17] W. Ke, G. Fang, Q. Liu, L. Xiong, P. Qin, H. Tao, J. Wang, H. Lei, B. Li, J. Wan, G. Yang, Y. Yan, *J. Am. Chem. Soc.* **2015**, *137*, 6730–6733.
- [18] K. Wang, Y. Shi, L. Gao, R. Chi, K. Shi, B. Guo, L. Zhao, T. Ma, *Nano Energy* **2017**, *31*, 424–431.
- [19] H. Zhou, Q. Chen, G. Li, S. Luo, T. B. Song, H. S. Duan, Z. Hong, J. You, Y. Liu, Y. Yang, *Science* **2014**, *345*, 542–546.
- [20] H. J. Snaith, A. Abate, J. M. Ball, G. E. Eperon, T. Leijtens, N. K. Noel, S. D. Stranks, J. T. Wang, K. Wojciechowski, W. Zhang, *J. Phys. Chem. Lett.* **2014**, *5*, 1511–1515.
- [21] Z. Song, A. Abate, S. C. Watthage, G. K. Liyanage, A. B. Phillips, U. Steiner, M. Graetzel, M. J. Heben, *Adv. Energy Mater.* **2016**, *6*, 1600846.
- [22] T. Leijtens, G. E. Eperon, S. Pathak, A. Abate, M. M. Lee, H. J. Snaith, *Nat. Commun.* **2013**, *4*, 2885–2892.
- [23] Q. Luo, H. Chen, Y. Lin, H. Du, Q. Hou, F. Hao, N. Wang, Z. Guo, J. Huang, *Adv. Funct. Mater.* **2017**, *27*, 1702090.
- [24] B. Li, Y. Li, C. Zheng, D. Gao, W. Huang, *RSC Adv.* **2016**, *47*, 38079–38091.
- [25] W. Hu, T. Liu, X. Yin, H. Liu, X. Zhao, S. Luo, Y. Guo, Z. Yao, J. Wang, N. Wang, H. Lin, Z. Guo, *J. Mater. Chem. A* **2016**, *5*, 1434–1441.
- [26] M. Grätzel, M. Grätzel, *Nature* **2001**, *414*, 338–344.
- [27] Z. Xiao, C. Bi, Y. Shao, Q. Dong, Q. Wang, Y. Yuan, C. Wang, Y. Gao, J. Huang, *Energy Environ. Sci.* **2014**, *7*, 2619–2613.
- [28] J. Y. Jeng, Y. F. Chiang, M. H. Lee, S. R. Peng, T. Guo, P. Chen, T. C. Wen, *Adv. Mater.* **2013**, *25*, 3727–3732.
- [29] P. Liang, C. Y. Liao, C. C. Chueh, F. Zuo, S. T. Williams, X. Xin, J. Lin, A. K. Y. Jen, *Adv. Mater.* **2014**, *26*, 3748–3654.
- [30] Y. Shao, Z. Xiao, C. Bi, Y. Yuan, J. Huang, *Nat. Commun.* **2014**, *5*, 5784–5791.
- [31] Y. Bai, Q. Dong, Y. Shao, Y. Deng, Q. Wang, L. Shen, D. Wang, W. Wei, J. Huang, *Nat. Commun.* **2016**, *7*, 12806–12815.
- [32] A. P. Grosvenor, B. A. Kobe, M. C. Biesinger, N. S. McIntyre, *Surf. Interface Anal.* **2004**, *36*, 1564–1574.
- [33] X. Yin, Z. Yao, Q. Luo, X. Dai, Y. Zhou, Y. Zhang, Y. Zhou, S. Luo, J. Li, N. Wang, H. Lin, *ACS. Appl. Mater. Interfaces* **2016**, *9*, 2439–2448.
- [34] Q. Luo, H. Ma, Y. Zhang, X. Yin, Z. Yao, N. Wang, J. Li, S. Fan, K. Jiang, H. Lin, *J. Mater. Chem. A* **2016**, *4*, 5569–5577.
- [35] C. Tao, S. Neutzner, L. Colella, S. Marras, A. R. S. Kandada, M. Gandini, M. D. Bastiani, G. Pace, L. Manna, M. Caironi, C. Bertarelli, A. Petrozza, *Energy Environ. Sci.* **2015**, *8*, 2365–2370.
- [36] W. Ke, Zhao, D. Xiao, C. Wang, C. Cimaroli, A. J. Grice, C. R. Yang, M. Li, Z. Jiang, C. M. Al-Jassim, K. Zhu, M. G. Kanatzidis, G. Fang, Y. Yan, *J. Mater. Chem. A* **2016**, *4*, 14276–14283.
- [37] Y. Zhang, P. Wang, X. Yu, J. Xie, X. Sun, H. Wang, J. Huang, L. Xu, C. Cui, M. Lei, D. Yang, *J. Mater. Chem. A* **2016**, *4*, 18509–18515.
- [38] J. W. Jung, C. C. Chueh, A. K. Y. Jen, *Adv. Mater.* **2015**, *27*, 7874–7880.
- [39] X. Yin, P. Chen, M. Que, Y. Xing, W. Que, C. Niu, J. Shao, *ACS Nano* **2016**, *10*, 3630–3636.
- [40] Q. Luo, H. Ma, F. Hao, Q. Hou, J. Ren, L. Wu, Z. Yao, Y. Zhou, N. Wang, K. Jiang, H. Lin, Z. Guo, *Adv. Funct. Mater.* **2017**, *27*, 1703068.
- [41] Q. Luo, Y. Zhang, C. Liu, J. Li, N. Wang, H. Lin, *J. Mater. Chem. A* **2015**, *3*, 15996–16004.
- [42] G. Niu, X. Guo, L. Wang, *J. Mater. Chem. A* **2015**, *3*, 8970–8980.

Manuscript received: October 6, 2017  
Version of record online: January 25, 2018